processes

MDPI

Article

A Nondimensional Physics-Informed Neural Network with CVT Adaptive Sampling for Electromagnetic Field Simulation in Electromagnetic Rail Launch Model

Yingbing Sun [1,2], Hao Xiong [1], Junwei Fan [1], Hongyang Wang [1], Shubo Hou [1], Xiuhong Hao [1,3,*] and Fenghe Wu [1,3]

[1] School of Mechanical Engineering, Yanshan University, Qinhuangdao 066004, China; sunyingbing@ysu.edu.cn (Y.S.); xionghao01@stumail.ysu.edu.cn (H.X.); jwfan@stumail.ysu.edu.cn (J.F.); why20030207@163.com (H.W.); shubohou@stumail.ysu.edu.cn (S.H.); risingwu@ysu.edu.cn (F.W.)
[2] Hebei Innovation Center for Equipment Lightweight Design and Manufacturing, Yanshan University, Qinhuangdao 066004, China
[3] State Key Laboratory of Crane Technology, Yanshan University, Qinhuangdao 066004, China
* Correspondence: hxhong@ysu.edu.cn

Abstract

A novel nondimensional physics-informed neural network (ND-PINN) with centroidal Voronoi tessellation (CVT) adaptive sampling (CVT-ND-PINN) is proposed to simulate the spatiotemporal evolution of the electromagnetic field induced by armature motion in electromagnetic launch systems in this paper. The proposed framework employs spatiotemporal coordinate scaling to reduce numerical disparities among the neural network inputs and alleviate scale-dependent optimization difficulties in electromagnetic field simulation. To further resolve high-gradient singularities associated with the velocity skin effect (VSE), a CVT sampling mechanism is introduced. Unlike uniform sampling, the CVT strategy dynamically concentrates collocation points in regions of rapid field variation, such as the armature-rail interface. Results demonstrate that the CVT-ND-PINN captures key physical phenomena with high fidelity, providing a physics-informed approximation of the electromagnetic field without the need for global mesh generation. Comparative analysis with the finite element method (FEM) shows that the maximum relative error is 3.42% (at 40 m/s and t = 5 ms). Although the prediction error increases with fewer collocation points, the CVT-ND-PINN framework maintains the ability to capture the main electromagnetic field characteristics, demonstrating the effectiveness of adaptive sampling in localized high-gradient regions. Furthermore, this study highlights the promising application potential of PINNs in the field of electromagnetic rail launch modeling.

Keywords: electromagnetic rail launch model; CVT-ND-PINN; extreme conditions of spacetime coupling; magnetic field distribution; velocity skin effect

Check for updates

Academic Editor: Iván García Kerdan

Received: 27 October 2026
Revised: 17 November 2026
Accepted: 24 November 2026
Published: 28 November 2026

Copyright: © 2026 by the authors. Licensee MDPI, Basel, Switzerland. This article is an open access article distributed under the terms and conditions of the Creative Commons Attribution (CC BY) license.

1. Introduction

Electromagnetic rail launching involves interacting electromagnetic, thermal, and mechanical phenomena. However, the present study focuses on electromagnetic field simulation under prescribed armature motion, without considering thermal–electrical coupling or mechanical deformation and their feedback effects on the electromagnetic field. The rails and armature are subjected to a combination of effects, including interference preload, electromagnetic forces, gouging erosion, frictional wear, high-speed electrical contact, and transient high-temperature exposure, all of which significantly degrade launch

performance [1–3]. A particularly notable phenomenon is the sliding electrical contact between the armature and rails, which gives rise to pronounced velocity skin effects due to the high-speed motion of the armature. This effect critically influences the distribution of magnetic fields and currents within the conductive components, making accurate modeling of the electromagnetic field essential for system design and optimization [4]. The intensity of the skin effect increases with armature velocity, further complicating the physical behavior. Given the transient and highly dynamic nature of the millisecond-level launch process, experimental investigations face considerable limitations. As a result, numerical simulation methods have become an indispensable tool for in-depth analysis and predictive modeling of electromagnetic launch systems.

Numerical simulation methods are widely employed in the electromagnetic field for their versatility and broad applicability, with the finite difference method (FDM) and finite element method (FEM) being the most prevalent. Researchers have utilized these approaches to investigate sliding electrical contact phenomena. Pang et al. [5] used the FDM to establish a two-dimensional electromagnetic field model and addressed armature motion through an upwinding factor for preserving grid topology while accounting for armature movement. Zhou et al. [6] applied an explicit FDM to solve magneto-thermal coupling equations, analyzing velocity skin effects in graphite-coated layered rails, Ti-Mo-Al layered armatures, and composite-structured armatures. M. Ghassemi et al. [7] employed the FDM to examine electromagnetic characteristics of armature-rail contact models considering metal liquefaction layers, subsequently extending this work to analyze electromagnetic force distribution on armature tail fins during dynamic launches, thereby validating FDM's applicability to sliding contact problems. FDM-based analyses have also revealed magnetic flux density, current density, and thermal distribution patterns under velocity skin effects. Commercial simulation software such as COMSOL, ANSYS, and LS-DYNA, which use the finite element method as the solver, are widely used to model the magnetic field distribution and current characteristics of electromagnetic rail launch models [8–10]. FEM typically discretizes domains into appropriate meshes and approximates partial differential equations using piecewise polynomials, though mesh quality critically impacts solution accuracy and computational costs. For motion-related challenges, the independent coordinate system method is commonly adopted to eliminate motion terms from coefficient matrices, ensuring matrix symmetry and avoiding oscillatory solutions at high speed [11–13]. However, the electromagnetic rail launch model presents unique computational hurdles: (1) Extended acceleration lengths (typically meter-scale) demand specialized domain treatments to prevent prohibitive computational resource consumption; (2) High-speed motion exacerbates numerical challenges in solving Maxwell's equations, as elevated Peclet numbers degrade matrix conditioning in discretized governing equations, inducing unphysical spurious oscillations; (3) Temporal scale disparities between electromagnetic and mechanical fields complicate time-step determination, while relative armature-rail motion introduces complex mesh deformation/distortion issues. These fundamental difficulties underscore the need for advanced numerical strategies in modeling high-speed electromagnetic rail launch models. What is more, the calculation time is proportional to mesh and model size, and larger models with finer mesh sizes can take hours, days, or even months to generate results.

The electromagnetic field solution for the electromagnetic rail launch model is typically governed by partial differential equations (PDEs). In contrast to conventional finite element analysis, researchers have proposed utilizing neural networks with approximate solutions to PDEs as an alternative to traditional numerical discretization methods. A physics-informed loss function is constructed to constrain the neural network to enable the acquisition of approximate PDE solutions through deep learning techniques [14]. This approach ensures consistency between observational data and physical laws, maintaining solution coherence.

Notably, physics-informed neural networks (PINNs) exhibit a mesh-free nature, eliminating dependence on grid quality and overcoming dimensional constraints [15]. Currently, PINNs have been extensively applied across diverse engineering domains with remarkable success [16–19]. For instance, they have been employed to investigate momentum and temperature distributions during the humidification of dry air, accounting for fluid properties, species interactions, thermal diffusion, convection, temperature field analysis, and metal additive manufacturing [20–22].

Electromagnetic applications using PINNs to an even wider range of nonlinear PDEs have been subsequently published. Khan et al. [23] used it to predict the electrostatic scalar potential and magnetic vector potential. Noakoasteen et al. [24] proposed a PINN model to predict the time evolution of field values in transient electromagnetic analysis. Beltran-Pulido et al. [25] solved the 2D magnetostatic problem with the PINN. Gong et al. [26] proposed a hot spot-driven PINN for magnetothermal analysis. Qi et al. [27] presented the coupling of the finite difference time-domain method for electromagnetic field simulation with a PINN-based solver for the heat equation. Jeong et al. [28] developed a physics-informed neural network for estimating a solution to a multi-physics problem involving electromagnetism, fluid dynamics, and heat transfer. Pu et al. [29] proposed a novel method based on PINN to calculate the PMC performance with high accuracy and low computational cost. Hou et al. [30] proposed an enhanced physical information neural network with data-physical drive fusion and used a special Poisson's equation solution in the magnetized region as a data drive during training. To the best of the authors' knowledge, there are no previous studies to realize the electromagnetic field simulation of the electromagnetic rail launch model with the help of PINN considering the speed skin effect.

Despite their advantages, standard PINNs still encounter two key obstacles in this application. The first is training instability under extreme scale disparity, where dimensional variables with substantially different magnitudes hinder network optimization. The second is insufficient local resolution in high-gradient regions, especially near the armature–rail interface and trailing-edge zones, where uniformly or randomly distributed collocation points often fail to provide adequate representation.

To address these challenges, this paper proposes a Centroidal Voronoi Tessellation-based nondimensional physics-informed neural network (CVT-ND-PINN) for electromagnetic field simulation in the electromagnetic rail launch model. Unlike conventional PINN approaches, the proposed framework combines spatiotemporal coordinate normalization with CVT adaptive collocation sampling to address both scale-related optimization difficulties and insufficient local sampling resolution. Specifically, nondimensionalization reduces the numerical scale disparity among input coordinates and improves the stability of neural network optimization, while the CVT strategy adaptively redistributes collocation points according to local PDE residual characteristics, enhancing the representation of high-gradient electromagnetic fields near the armature–rail interface. The combination of these two strategies provides complementary improvements in global optimization stability and local field resolution, enabling more accurate reconstruction of electromagnetic field distributions associated with the velocity skin effect. Based on the electromagnetic governing equations and corresponding boundary/interface conditions, the proposed framework achieves continuous electromagnetic field approximation without requiring global mesh generation.

Unlike adaptive collocation strategies that directly select candidate points based on large PDE residuals, the proposed framework employs a CVT adaptive sampling mechanism based on the PDE residual distribution. By constructing a spatial density function and iteratively updating the density-weighted centroids of Voronoi regions, collocation points are redistributed toward high-residual regions while maintaining global domain

coverage with a fixed number of points. Furthermore, CVT adaptive sampling is integrated with spatiotemporal coordinate scaling to improve local sampling resolution and alleviate numerical optimization difficulties caused by disparities in input coordinate scales, while FEM reference data provide supplementary constraints. Through these complementary strategies, CVT-ND-PINN enables more accurate reconstruction of complex magnetic field distributions near the armature–rail interface under the velocity skin effect.

The main contributions of this work are summarized as follows:

(1) A nondimensional PINN framework is developed for electromagnetic field simulation in the electromagnetic rail launch model, aiming to improve training stability by reducing numerical scale disparities in spatiotemporal coordinates.
(2) A CVT adaptive collocation sampling strategy is integrated with the nondimensional PINN framework to improve the representation of localized high-gradient electromagnetic fields associated with the velocity skin effect. This integration addresses both scale-related optimization difficulties and insufficient local sampling resolution.
(3) The integrated CVT-ND-PINN framework is evaluated against finite element simulations under different velocities, demonstrating its capability to reproduce electromagnetic field distributions and capture the velocity skin effect within the considered two-dimensional model.

The remainder of this paper is organized as follows. Section 2 introduces the electromagnetic rail launch model structure, governing equations, boundary conditions, nondimensionalization method, CVT structure, and PINN fundamentals. Section 3 presents the construction of the proposed CVT-ND-PINN framework. Section 4 discusses the numerical results and compares the proposed method with FEM and alternative sampling strategies. Finally, Section 5 concludes the paper.

2. Background

2.1. The Main Structure and Principle of the Electromagnetic Rail Launch Model

A typical electromagnetic rail launch model comprises two parallel conductive rails, a movable armature, and a high-power pulsed power supply, as illustrated in Figure 1. During operation, the armature maintains sliding electrical contact with the rails and moves along them under the influence of the generated electromagnetic forces. The pulsed current enters through one rail, passes through the armature, and returns via the other rail, thereby forming a closed-loop circuit. This current flow generates a magnetic flux density (B) around the rails. The interaction between the magnetic field and the current induces a Lorentz force (F) that accelerates the armature along the direction of the rails.

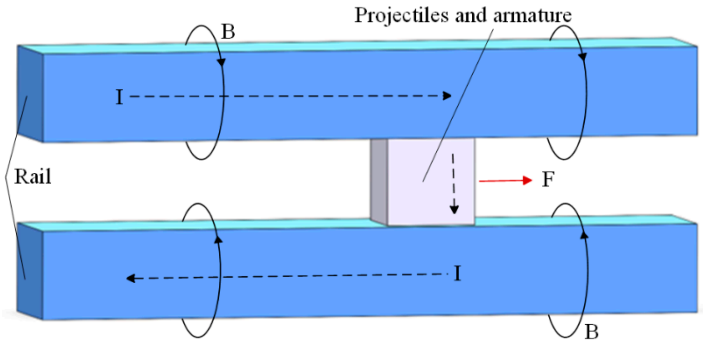


Figure 1. The electromagnetic rail launch model structure diagram.

In the 3D electromagnetic rail launch model, the magnetic field distribution comprises components in all three spatial directions. Due to the high-speed motion of the armature,

the electromagnetic field exhibits strong dynamic characteristics, leading to a significantly complex computational problem. To facilitate analysis while retaining essential physical features, a 2D modeling approach is commonly adopted. Specifically, a 2D line-source model can be established within a rectangular coordinate system, enabling the derivation of governing equations and the definition of boundary conditions in a more tractable manner. Based on the hierarchical modeling strategy, the direction of the magnetic field within the electromagnetic rail launch model is aligned predominantly along the *z*-axis. Therefore, the 3D structure can be effectively reduced to a 2D model in the xoy plane, as illustrated in Figure 2. Given that both the rails and the armature exhibit symmetry with respect to the xoy plane, only half of the 2D model needs to be considered for simulation purposes. The simplified computational domain is shown in Figure 3. Furthermore, according to the hierarchical modeling methodology, the reduced 2D model is divided into two primary regions and nine distinct boundaries. This partitioning facilitates precise representation of material interfaces and boundary conditions in subsequent numerical or learning-based simulations.

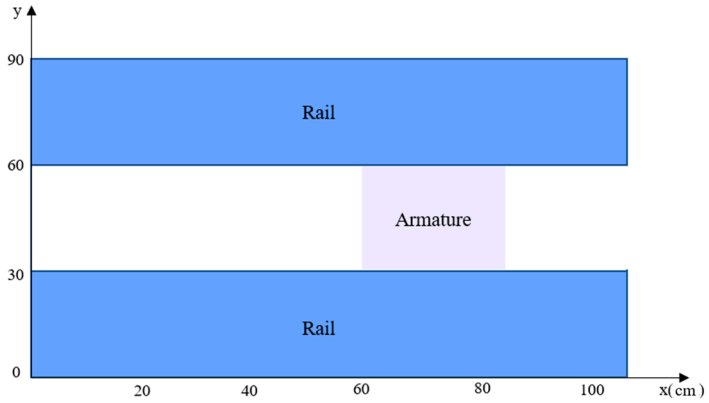


Figure 2. Two-dimensional model of the electromagnetic rail launch model.

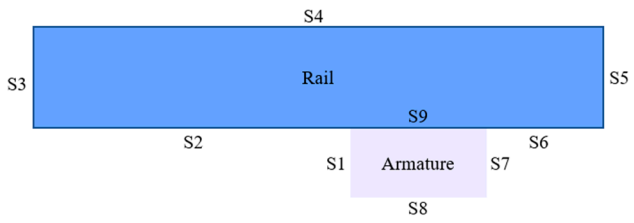


Figure 3. Simplified 2D model of the electromagnetic rail launch model.

In the process of research, it is assumed that the armature and the track are in good initial contact with no contact resistance. In the process of armature movement, the armature and the track are rigid bodies, and the deformation of the two is not considered, and the armature is not damaged. The electrical resistivity and other physical parameters of the armature and guide rail do not change with the change in temperature. These simplifying assumptions impose certain limitations on the applicability of the present model. Neglecting contact resistance excludes the effects of imperfect electrical contact and the associated localized current concentration at the armature–rail interface. The rigid-body assumption prevents the model from accounting for contact geometry changes caused by material deformation, while constant material properties exclude the influence of temperature-dependent resistivity variations induced by Joule heating. Consequently, the present model primarily describes electromagnetic field characteristics under idealized contact and material conditions.

2.2. Governing Equations and Boundary Conditions

It is assumed that the armature is in good contact with the guide rail, and x is the direction of armature movement. During the movement of the armature, both the armature and the rail are rigid bodies, and their deformation and wear are not considered. The physical parameters, such as resistivity, of both do not change with temperature. From Faraday's law and Ampere's Law expressed in the differential form of Maxwell's equations, the following can be obtained:

$$\nabla \times \boldsymbol{E} = -\frac{\partial \boldsymbol{B}}{\partial t} \tag{1}$$

$$\nabla \times \boldsymbol{H} = \boldsymbol{J} \tag{2}$$

Considering the change caused by velocity, according to Ohm's law:

$$\boldsymbol{J} = \sigma(\boldsymbol{E} + \boldsymbol{v} \times \boldsymbol{B}) \tag{3}$$

The vector magnetic diffusion equation is obtained by sorting and transforming the above equation:

$$\nabla^2 \boldsymbol{B} = \mu\sigma \frac{\partial \boldsymbol{B}}{\partial t} - \mu\sigma \nabla \times (\boldsymbol{v} \times \boldsymbol{B}) \tag{4}$$

The governing equation of the electromagnetic field in the motion domain is as follows:

$$\sigma\mu \frac{\partial B_z}{\partial t} + \sigma\mu v_x \frac{\partial B_z}{\partial x} = \frac{\partial^2 B_z}{\partial x^2} + \frac{\partial^2 B_z}{\partial y^2} \tag{5}$$

The governing equation of the static domain electromagnetic field is as follows:

$$\sigma\mu \frac{\partial B_z}{\partial t} = \frac{\partial^2 B_z}{\partial x^2} + \frac{\partial^2 B_z}{\partial y^2} \tag{6}$$

In the whole computational domain, the initial conditions are as follows:

$$B_z(0) = 0 \tag{7}$$

The boundary conditions are as follows:

$$\begin{cases} B_z = 0, S_4, S_5, S_6, S_7 \\ B_z = B_{z0}(t) = \mu J, S_1, S_2 \\ \frac{\partial B_z}{\partial x} = 0, S_3 \\ \frac{\partial B_z}{\partial y} = 0, S_8 \end{cases} \tag{8}$$

The condition of the interface between armature and track is as follows:

$$\begin{cases} B_{z1} = B_{z2} \\ \frac{1}{\mu_1}\frac{\partial B_{z1}}{\partial y} = \frac{1}{\mu_2}\frac{\partial B_{z2}}{\partial y} \end{cases}, S_9 \tag{9}$$

Here, σ, μ, v_x are the electrical conductivity, magnetic permeability, and motion speed of the material, respectively; B_z is the intensity of magnetic induction, and only the directional component exists for two-dimensional problems; J represents the applied equivalent line current density, whose direction is parallel to the solution domain plane. For boundary S_1, J exists only in the y-direction, while for boundary S_2, J exists only in the x-direction. The electromagnetic induction intensities applied at the boundaries S_1 and S_2 of the model are used to equivalently introduce current density excitation. As illustrated in Figure 3, boundaries S1–S9 are defined according to the geometric configuration of the rail and armature. S1 represents the left boundary of the armature, while S2 corresponds to the lower boundary of the rail on the left side of the contact region. These two boundaries are subjected to prescribed magnetic flux density conditions to introduce equivalent current

excitation into the electromagnetic model. S3, S4, S5, and S6 represent the left, upper, right, and lower-right external boundaries of the rail, respectively, where homogeneous Dirichlet conditions are imposed by setting the magnetic flux density to zero. S7 and S8 correspond to the right and bottom boundaries of the armature, respectively, where homogeneous Neumann conditions are applied by setting the normal derivatives of the magnetic flux density to zero. S9 represents the contact interface between the rail and armature, where the continuity conditions given in Equation (9) are imposed to describe the electromagnetic field transmission between the two conductive materials. These boundary conditions define the electromagnetic constraints of the simplified two-dimensional computational model.

2.3. Nondimensionalization Approach

The electromagnetic rail launch model involves spatial and temporal variables with different characteristic scales, which may introduce numerical difficulties when their dimensional coordinate values are directly used as neural network inputs. In this study, spatiotemporal coordinate scaling is adopted to reduce the numerical disparities among the input variables, rather than performing full nondimensionalization of all electromagnetic quantities. Specifically, a characteristic length and a characteristic time are introduced to transform the spatial and temporal coordinates into dimensionless variables, as follows:

$$x^* = x/L, y^* = y/L, t^* = t/\tau \tag{10}$$

By rescaling the spatiotemporal coordinates, this approach aims to reduce input-scale disparities and improve the numerical stability of PINN optimization for electromagnetic field simulation. Therefore, the control equation is modified to the following:

$$\frac{\sigma\mu}{\tau}\frac{\partial B_z}{\partial t^*} + \frac{\sigma\mu v_x}{L}\frac{\partial B_z}{\partial x^*} = \frac{1}{L^2}\frac{\partial^2 B_z}{\partial x^{*2}} + \frac{1}{L^2}\frac{\partial^2 B_z}{\partial y^{*2}} \tag{11}$$

In this study, spatiotemporal coordinate scaling is introduced to reduce numerical disparities among the neural network inputs. As defined in Equation (10), L and τ denote the characteristic length and characteristic time, respectively. The characteristic time is set to $\tau = 5$ ms, corresponding to the representative electromagnetic field evaluation time used for comparing different velocity conditions. This choice maps the evaluation time to $t^* = 1$ and provides a consistent temporal reference for the simulations. The characteristic length is determined through the coordinate-scale comparison presented in Section 4. It should be noted that the coordinate transformation does not involve complete nondimensionalization of the electromagnetic quantities, and B_z retains its physical unit of tesla (T). According to the chain rule, the temporal first-order derivative, spatial first-order derivatives, and spatial second-order derivatives introduce scaling factors of $\frac{1}{\tau}$, $\frac{1}{L}$, and $\frac{1}{L^2}$, respectively. When the dimensional parameters are expressed in consistent SI units, the coefficients $\frac{\sigma\mu}{\tau}$, $\frac{\sigma\mu v}{L}$, and $\frac{1}{L^2}$ all have units of m^{-2}. Therefore, every term in Equation (11) has units of T/m^2, confirming the dimensional consistency of the transformed governing equation.

The influence of coordinate scaling on PINN optimization can be further understood from the chain rule. As shown in Equation (11), the first-order spatial derivative terms are multiplied by $\frac{1}{L}$, whereas the second-order spatial derivative terms are multiplied by $\frac{1}{L^2}$. Consequently, the selection of the characteristic length affects the relative numerical magnitudes of the convection and diffusion terms in the PDE residual. For the mean-squared PDE residual loss, its gradient with respect to the network parameters is given by $\nabla_\theta L = \left(\frac{2}{N_f}\right)\sum_{i=1}^{N_f} R_{\theta,i}\nabla_\theta R_{\theta,i}$. Therefore, changes in the coordinate scale can affect both the PDE residual values and their gradient contributions during optimization. When the numerical coordinate scale is inappropriate, these effects may lead to imbalanced optimization among the PDE residual and other loss components. In addition, excessively

large network inputs may increase the likelihood of Tanh activation saturation, further hindering gradient propagation.

2.4. Centroidal Voronoi Tessellation (CVT) for Adaptive Collocation Sampling

The Centroidal Voronoi Tessellation (CVT) is a geometric method widely used for distributing points in a way that optimizes their spatial coverage, particularly in regions with varying density. In the context of this study, CVT is employed as a local adaptive collocation sampling strategy to address the challenges of high-gradient regions in the electromagnetic rail launch model simulations, particularly those induced by the velocity skin effect (VSE).

For a given domain $\Omega \in \mathbb{R}^n$ and a set of k generator points $\{z_i\}$, the space is partitioned into k corresponding Voronoi regions $\{V_i\}_{i=1}^k$, such that $\Omega = \cup_{i=1}^k V_i$. Each region V_i is defined as follows:

$$V_i = \left\{ x \in \Omega \middle| \|x - z_i\| < \left\|x - z_j\right\|, j \neq i \right\} \tag{12}$$

Here, z_i is the generator point associated with the Voronoi region V_i. A Voronoi tessellation is said to be centroidal if each generator point z_i within its region V_i coincides with the center of mass z_i^* of that region, defined as follows:

$$z_i^* = \frac{\int_{V_i} x\rho(x)dx}{\int_{V_i} \rho(x)dx} \tag{13}$$

In the proposed CVT adaptive sampling framework, the density function is constructed based on the magnitude of the PDE residual predicted by the current neural network. A residual-based density function can be defined as follows:

$$\rho(x) = \rho_{\min} + \left(\frac{|R_\theta(x)|}{\overline{R}_\theta + \varepsilon} \right)^p \tag{14}$$

Here, $R_\theta(x)$ represents the PDE residual at a candidate sampling location, $\overline{R}_\theta$ denotes the mean absolute residual over the candidate points, $\rho_{\min} > 0$ is a background density ensuring global domain coverage, $\varepsilon > 0$ is a small constant introduced to avoid division by zero, and p controls the sensitivity of the sampling density to the residual magnitude. Regions with larger PDE residuals are therefore assigned higher sampling densities.

The CVT adaptive sampling procedure is implemented through an iterative residual-based collocation-point redistribution strategy. The parameters in Equation (14) are set to $\rho = 0.1$, $p = 2$, and $\varepsilon = 1 \times 10^{-6}$. In total, 20,000 candidate points are used to evaluate the PDE residual distribution and numerically approximate the density-weighted centroids of the Voronoi regions. These candidate points are auxiliary evaluation points used for CVT adaptation and are not included as additional collocation points in the PINN training loss. The actual training collocation points serve as the Voronoi generators, with their total number prescribed according to the corresponding experimental configuration. The PINN is initially trained for 600 iterations to obtain a preliminary approximation of the electromagnetic field. Thereafter, the CVT adaptation is performed every 100 PINN training iterations. During each update, the PDE residuals are evaluated at the candidate points using the current neural network, and the sampling density function is recalculated according to Equation (14). The Voronoi regions are constructed using the current training collocation points, which are then iteratively relocated toward the density-weighted centroids defined in Equation (13). The convergence criterion is based on the maximum generator displacement normalized by the characteristic size of the computational domain, with a tolerance of 1×10^{-3}. Each CVT update terminates when the convergence criterion is satisfied or when 20 internal centroidal iterations have been completed. The updated collocation points are

subsequently used for PINN training while their total number remains unchanged. This procedure enables adaptive redistribution of collocation points toward regions with larger PDE residuals while maintaining coverage of the computational domain.

2.5. Physics-Informed Neural Networks

The PINN model is usually composed of a deep neural network, and its core is to add the governing equation and boundary conditions to the loss function to construct a neural network that conforms to physical laws. The trained neural network can not only approximate the real physical data, but also satisfy the physical characteristics embodied by PDEs. Suppose there exists a typical nonlinear time-varying partial differential equation with the following expression:

$$f(x,t;\frac{\partial u}{\partial x_1},\frac{\partial u}{\partial x_2},\cdots,\frac{\partial u}{\partial x_n};\frac{\partial u}{\partial x_1^2},\cdots,\frac{\partial u}{\partial x_1 \partial x_n};\cdots;\lambda)=0, x\in\Omega, t\in[0,T] \tag{15}$$

$$u(x,0)=h(x), x\in\Omega \tag{16}$$

$$u(x,t)=g(x,t), x\in\partial\Omega, t\in[0,T] \tag{17}$$

Here, Ω and $\partial\Omega$ represent the spatial domain and boundary, respectively. $x\in\Omega$ and $t\in[0,T]$ represent the spatial and temporal coordinates, respectively. f represents the specific form of PDEs, including the differential operator $(\frac{\partial u}{\partial x_1},\cdots,\frac{\partial u}{\partial x_n})$ and parameter $\lambda=(\lambda_1,\lambda_2,\cdots,\lambda_n)$; $u(x,0)$ and $u(x,t)$ represent solutions under initial condition $h(x)$ and boundary condition $g(x,t)$, which can be arbitrary boundary conditions, such as Dirichlet, Neumann, and Robin.

In the underlying framework of PINN, we approximate the neural network of solution $u(x,t)$ as $\hat{u}(x,t;\theta)$, where denotes a set of network parameters. Usually, the feedforward multi-layer neural network consists of an input layer, multiple hidden layers, and an output layer, and its structure is shown in Figure 4. The neural network can be expressed as follows:

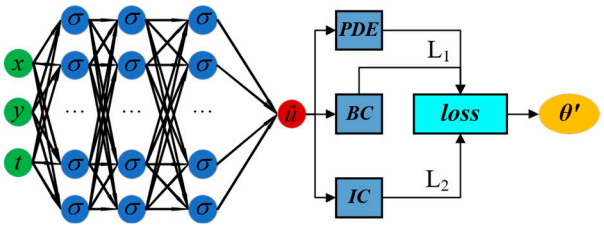


Figure 4. PINN training model.

Input layer:

$$\hat{u}^{[1]}=x \tag{18}$$

Hidden layer:

$$\hat{u}^{[m]}=\delta(W^{[m]}\hat{u}^{[m-1]}+b^{[m]}) \quad m=2,3,\cdots,M-1 \tag{19}$$

Output layer:

$$\hat{u}^{[M]}=\delta(W^{[M]}\hat{u}^{[M-1]}+b^{[M]}) \tag{20}$$

Here, δ is the activation function; usually, sigmoid, ReLU, and tan are used. $W^{[m]}$ and $b^{[m]}$ represent the weight parameters and bias terms of each layer in the neural network. $\theta=\{W^{[m]},b^{[m]}\}$ denotes the set of all weight matrices and bias vectors in the neural network.

PINN optimizes the problem by repeatedly adjusting the parameters of a trainable model such as $W^{[m]}$ and $b^{[m]}$ using methods such as gradient descent to solve a system of partial differential equations and minimize a loss function. PINN can enhance the expressive

power of data by embedding physical prior knowledge into the loss function, which is defined as follows:

$$L(\theta;N) = L_{PDE}(\theta;N_p) + L_{BC}(\theta;N_b) + L_{IC}(\theta;N_i) \tag{21}$$

Here, $\lambda = \{\lambda_p,\lambda_b,\lambda_i,\lambda_d\}$ is the loss weight parameter. L_{PDE}, L_{BC} and L_{IC} are defined as follows:

$$L_{PDE}(\theta;N_p) = \frac{1}{|N_p|}\sum_{j=1}^{N_p}\left\|f(x_p^j,t_p^j;\theta)\right\|^2 \tag{22}$$

$$L_{BC}(\theta;N_b) = \frac{1}{|N_b|}\sum_{j=1}^{N_b}\left\|\hat{u}(x_b^j,t_b^j;\theta) - g_b^j\right\|^2 \tag{23}$$

$$L_{IC}(\theta;N_i) = \frac{1}{|N_i|}\sum_{j=1}^{N_i}\left\|\hat{u}(x_i^j,0;\theta) - h_i^j\right\|^2 \tag{24}$$

Here, the first loss term L_{PDE} means the PDE residuals evaluated at collocation points $\left\{x_p^j,t_p^j\right\}_{j=1}^{N_p}$ that are randomly sampled inside the domain Ω; The second loss term L_{BC} uses a set of training data $\left\{x_b^j,t_b^j\right\}_{j=1}^{N_b}$ to enforce boundary conditions; Similarly, the third loss term L_{IC} ensures that the training points $\left\{x_i^j,t_i^j\right\}_{i=1}^{N_i}$ meet the initial conditions. N_p, N_b, and N_i denote the total number of different types of sampling points in PINN training, respectively. Specifically, N_p is the number of internal sampling points used to calculate the PDE residual, N_b is the number of boundary condition sampling points, and N_i is the number of initial condition sampling points.

3. PDE Solution of the Electromagnetic Rail Launch Model Based on CVT-ND-PINN

3.1. Overall Framework of the CVT-ND-PINN

In this study, a fully connected deep neural network is employed to construct the electromagnetic field solver. The network takes the nondimensionalized spatial–temporal coordinates as inputs and predicts the corresponding field variable over the continuous computational domain. Compared with conventional mesh-based solvers, this approach directly approximates the PDE solution without requiring domain-wide discretization. The proposed CVT-ND-PINN consists of three tightly coupled components: a nondimensional PDE formulation, a physics-informed neural network architecture, and a CVT adaptive collocation sampling strategy.

The workflow is as follows. First, the nondimensionalized coordinates (x, y, t) are fed into the neural network. Second, the required first-order and second-order derivatives are obtained through automatic differentiation. Third, the PDE residuals, boundary and interface constraints, and initial-condition constraints are combined into a composite loss function. Finally, the network parameters are optimized using the Adam algorithm with a two-stage learning-rate schedule for a prescribed total of 2000 training iterations.

The proposed framework introduces a more physically meaningful sample allocation mechanism, enabling the network to better capture the localized electromagnetic field distortion caused by armature motion and the velocity skin effect.

3.2. Establishing the Loss Function

According to Equations (5), (6) and (22), the PDE loss can be expressed as follows:

$$L_{\mathrm{PDE1}}(\theta;N_p) = \frac{1}{|N_p|}\sum_{j=1}^{N_p}\left\|\sigma\mu\frac{\partial\hat{B}_z(x_j,t_j)}{\partial t} + \sigma\mu v_x\frac{\partial\hat{B}_z(x_j,t_j)}{\partial x} - \frac{\partial^2\hat{B}_z(x_j,t_j)}{\partial x^2} - \frac{\partial^2\hat{B}_z(x_j,t_j)}{\partial y^2}\right\|^2 \tag{25}$$

$$L_{\mathrm{PDE2}}(\theta;N_p)=\frac{1}{|N_p|}\sum_{j=1}^{N_p}\left\|\sigma\mu\frac{\partial\hat{B}_z(x_j,t_j)}{\partial t}-\frac{\partial^2\hat{B}_z(x_j,t_j)}{\partial x^2}-\frac{\partial^2\hat{B}_z(x_j,t_j)}{\partial y^2}\right\|^2 \tag{26}$$

According to Equations (8), (9) and (23), the boundary condition loss can be expressed as follows:

$$\begin{cases} L_{\mathrm{BC1}}(\theta;N_{b1})=\dfrac{1}{|N_{b1}|}\sum\limits_{j=1}^{N_{b1}}\left\|\hat{B}_z(x_j,t_j)-\mu J\right\|^2, L_{BC2}(\theta;N_{b2})=\dfrac{1}{|N_{b2}|}\sum\limits_{j=1}^{N_{b2}}\left\|\hat{B}_z(x_j,t_j)-\mu J\right\|^2 \\ L_{\mathrm{BC3}}(\theta;N_{b3})=\dfrac{1}{|N_{b3}|}\sum\limits_{j=1}^{N_{b3}}\left\|\dfrac{\partial\hat{B}_z(x_j,t_j)}{\partial x}\right\|^2, L_{BC4}(\theta;N_{b4})=\dfrac{1}{|N_{b4}|}\sum\limits_{j=1}^{N_{b4}}\left\|\hat{B}_z(x_j,t_j)\right\|^2 \\ L_{\mathrm{BC5}}(\theta;N_{b5})=\dfrac{1}{|N_{b5}|}\sum\limits_{j=1}^{N_{b5}}\left\|\hat{B}_z(x_j,t_j)\right\|^2, L_{BC6}(\theta;N_{b6})=\dfrac{1}{|N_{b6}|}\sum\limits_{j=1}^{N_{b6}}\left\|\hat{B}_z(x_j,t_j)\right\|^2 \\ L_{\mathrm{BC7}}(\theta;N_{b7})=\dfrac{1}{|N_{b7}|}\sum\limits_{j=1}^{N_{b7}}\left\|\hat{B}_z(x_j,t_j)\right\|^2, L_{BC8}(\theta;N_{b8})=\dfrac{1}{|N_{b8}|}\sum\limits_{j=1}^{N_{b8}}\left\|\dfrac{\partial\hat{B}_z(x_j,t_j)}{\partial y}\right\|^2 \\ L_{\mathrm{BC9}}(\theta;N_{b9})=\dfrac{1}{|N_{b9}|}\sum\limits_{j=1}^{N9}\left\|\hat{B}_{z1}(x_j,t_j)-\hat{B}_{z2}(x_j,t_j)\right\|^2+\dfrac{1}{|N_{b9}|}\sum\limits_{j=1}^{N9}\left\|\dfrac{1}{\mu_1}\dfrac{\partial\hat{B}_{z1}(x_j,t_j)}{\partial y}-\dfrac{1}{\mu_2}\dfrac{\partial\hat{B}_{z2}(x_j,t_j)}{\partial y}\right\|^2 \end{cases} \tag{27}$$

According to Equations (7) and (24), the initial condition loss can be expressed as follows:

$$L_{\mathrm{IC}}(\theta;N_i)=\frac{1}{|N_i|}\sum_{j=1}^{N_i}\left\|\hat{B}_z(x_j,0)\right\|^2 \tag{28}$$

The loss of data items is as follows:

$$L_{\mathrm{DATA}}(\theta;N_i)=\frac{1}{|N_d|}\sum_{j=1}^{N_d}\left\|\hat{B}_z(x_j,t_j)-B_j\right\|^2 \tag{29}$$

The reference magnetic field values used in the data-driven loss calculation are obtained through finite element method (FEM) simulations under the corresponding operating conditions. At each speed condition, 200 reference points are selected at the 5 ms reporting and evaluation time, located in the local high-gradient region near the trailing edge of the armature, to provide supplementary spatial constraints. The FEM magnetic field values at these positions are incorporated into the data-driven loss model to improve the prediction accuracy of the local high-gradient areas.

According to Equations (25)–(29), the total loss function can be expressed as follows:

$$L(\theta;N)=\omega_1L_{\mathrm{PDE}}(\theta;N_p)+\omega_2L_{\mathrm{BC1}}(\theta;N_{b1})+\cdots+\omega_{11}L_{\mathrm{IC}}(\theta;N_i)+\omega_{12}L_{\mathrm{DATA}}(\theta;N_d) \tag{30}$$

All weighting coefficients in the total loss function are set to 1. Each loss component is calculated as the mean squared error over its corresponding sampling points. The PDE residual losses enforce the electromagnetic governing equations in the moving and stationary regions, while the boundary and interface condition losses constrain the electromagnetic field on the corresponding boundaries and material interfaces. The initial condition loss ensures consistency with the prescribed initial magnetic field, and the data-driven loss provides supplementary supervision using the FEM reference values. During training, all loss components are combined into the total objective function, and the network parameters are iteratively updated through automatic differentiation and backpropagation. This formulation incorporates the governing equations, initial and boundary conditions, and reference data into a unified optimization framework.

The spatial and temporal derivatives can be computed using automatic differentiation (AD). Once the mechanical structure and material parameters of the electromagnetic rail launch model are determined, the other physical parameters are also determined, so that the calculation process of the loss function is easy.

Consequently, solving the governing equations is reformulated as an optimization problem in which the neural network parameters are iteratively updated through backpropagation to minimize the physics-informed loss function.

3.3. Establishing the PINN Model

The physics-informed neural network (PINN) algorithm is employed to solve Maxwell's equations with the aim of achieving accurate simulations of the magnetic field distribution in the electromagnetic rail launch model. The construction of the PINN model is based on the fundamental governing equations and corresponding boundary conditions.

The overall PINN framework for the electromagnetic rail launch model is illustrated in Figure 5, which can be divided into three main components: the deep neural network, automatic differentiation (AD), and the integration of physical information. In this framework, the architecture of the deep neural network, as well as the mapping relationship between input and output variables, must be explicitly defined. Automatic differentiation is then applied to compute the required partial derivatives of the network outputs with respect to the input coordinates. Finally, the network parameters are optimized by minimizing a carefully designed loss function.

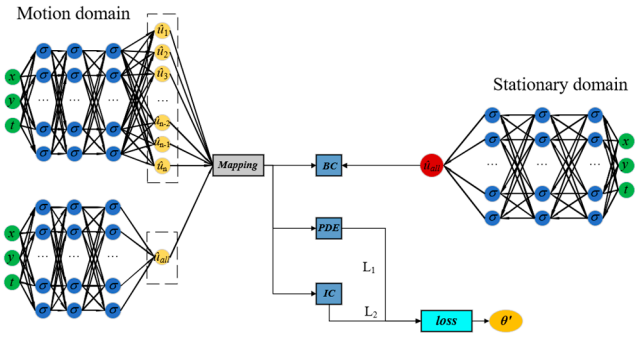


Figure 5. PINN model of the electromagnetic rail launch model.

In the constructed deep neural network, the input variables include spatial variables x, y, and temporal variables t. In the process of AD, the first and second derivatives of the network output with respect to the input can be calculated automatically to realize the high-precision approximation of the partial differential term. In the process of introducing physical information, the aforementioned governing equations and boundary conditions will be used as constraints in the network training.

To provide a clear and reproducible description of the proposed CVT-ND-PINN framework, the network architecture and key training parameters are summarized in Table 1. The table includes the input and output variables, number of hidden layers, neurons per layer, activation function, optimization algorithm, and other relevant training configurations. These parameters define the neural network implementation used for electromagnetic field approximation and physics-informed optimization.

The CVT-ND-PINN framework is trained using the Adam optimizer with a two-stage dynamic learning-rate schedule. During the first 600 iterations, linear warmup is applied to gradually increase the learning rate from 0 to 1×10^{-4}, thereby mitigating abrupt parameter updates during the initial training stage. During the subsequent 1400 iterations, cosine annealing is employed to smoothly decrease the learning rate from 1×10^{-4} to approximately zero, allowing progressively smaller parameter updates during the later stages of optimization. A fixed training budget of 2000 iterations is adopted as the stopping criterion. This setting ensures a consistent training budget across different simulation conditions and sampling strategies. All neural network computations, including forward propagation,

loss evaluation, and automatic differentiation, are performed using 64-bit double-precision floating-point arithmetic (float64). The framework is implemented in Python 3.10 using PyTorch 2.2, and the training process is performed on an NVIDIA GeForce RTX 3090 GPU equipped with 24 GB of memory.

Table 1. Neural network architecture and training parameters of the CVT-ND-PINN framework.

Parameter	Configuration
Network type	Fully connected feedforward neural network
Input variables	(x^*, y^*, t^*)
Output variable	Bz
Number of hidden layers	4
Neurons per hidden layer	64
Activation function	Tanh
Optimization algorithm	Adam
Weight initialization	Xavier uniform initialization
Training iterations	2000

3.4. Relevant Physical Parameters and Materials

The relevant physical material parameters of the electromagnetic rail launch model adopted by the PINN model are shown in Tables 2 and 3. The track and armature materials are copper and aluminum, respectively.

Table 2. Rail material parameters.

Parameters	Value	Unit
Density	8900	kg/m^3
Electrical conductivity	5.8 × 107	S/m
Relative permeability	1	

Table 3. Armature material parameters.

Parameters	Value	Unit
Density	2700	kg/m^3
Electrical conductivity	3.5 × 107	S/m
Relative permeability	1	

4. Results and Discussion

To establish the numerical reliability of the FEM reference solution, a mesh-convergence study was conducted for the two-dimensional electromagnetic rail launch model. Since the magnetic field gradients are particularly pronounced near the trailing edge of the armature and the armature–rail interface under high-velocity conditions, the case of 40 m/s at t = 5 ms was selected as the representative condition for the convergence analysis. Four progressively refined triangular meshes containing 24,000, 48,000, 96,000, and 152,000 elements were considered while maintaining identical geometric configurations, material properties, boundary conditions, and operating conditions. The relative changes in magnetic flux density between successive mesh levels were evaluated in both the entire conductive domain and the localized high-gradient region near the armature–rail interface. The corresponding mesh-convergence results are presented in Table 4. The 152,000-element mesh is the FEM reference for every comparison below. Relative to the 96,000-element mesh, it changes Bz by 0.54% over the conductive domain and by 0.80% in the local high-gradient region.

Table 4. FEM mesh-convergence results.

Number of FEM Elements	Relative Change in Entire Domain	Relative Change in Local High-Gradient
24,000		
48,000	2.48%	3.62%
96,000	1.18%	1.67%
152,000	0.54%	0.80%

When the excitation magnetic field is set to B = 12.56 T, the finite element simulation results of the electromagnetic field in different scale ranges under the static conditions of the electromagnetic rail launch model are shown in Figure 6. It should be emphasized that the three coordinate-scale comparisons are based on the same physical geometry of the electromagnetic rail launch model, with identical material properties and boundary conditions. The differences among these cases arise from the numerical representation of the spatial coordinates rather than changes in the physical dimensions. To investigate the influence of spatial coordinate scaling, three representative characteristic lengths, L = 100 cm, 10 cm, and 1 cm, are considered. These values cover different characteristic length scales of the electromagnetic rail launch model. The length of 100 cm is comparable to the overall physical domain length of 110 cm, whereas 1 cm corresponds approximately to the characteristic magnetic diffusion length scale estimated from the governing diffusion equation at 5 ms. Using the electrical conductivities and relative permeabilities in Tables 2 and 3, the estimated diffusion length scales are approximately 0.83 cm for copper and 1.07 cm for aluminum. The intermediate length of 10 cm provides a logarithmically spaced candidate between the global geometric and local diffusion scales. According to the coordinate transformation in Equation (10), these three characteristic lengths correspond to the dimensionless x-coordinate ranges of [0, 1.1], [0, 11], and [0, 110], respectively, for the same physical length of 110 cm. The spatial coordinates in each case are scaled consistently, while the governing equations retain the corresponding derivative scaling coefficients. These comparisons are intended to evaluate the sensitivity of PINN training to different coordinate scales and to demonstrate the importance of selecting an appropriate characteristic length for numerical optimization.

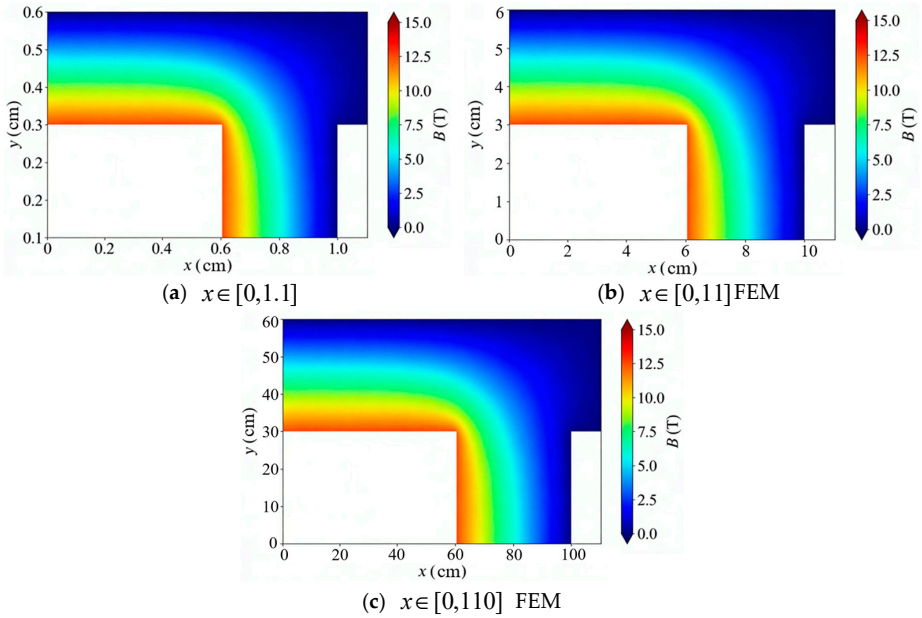


Figure 6. The simulation result using FEM.

However, the PINN simulation analysis and absolute error results are shown in Figure 7. The results show that, compared with the finite element simulation results, the magnetic field simulation error is the smallest when the x-axis range is $[0, 11]$. When the x-axis range is $[0, 1.1]$, the trend remains consistent, but the error is significantly larger. When the same physical problem is represented using the numerical coordinate range $[0, 110]$, the PINN exhibits substantial prediction errors, indicating difficulties in the corresponding optimization process. As discussed in Section 2.3, an inappropriate coordinate scale can alter the relative gradient contributions of different loss terms and may cause activation saturation, thereby hindering the approximation of localized high-gradient electromagnetic fields. In contrast, the $[0, 11]$ coordinate representation provides better agreement with the FEM reference under the investigated conditions. These results support the importance of appropriate coordinate scaling for PINN optimization. All CVT-ND-PINN results below therefore use L = 10 cm.

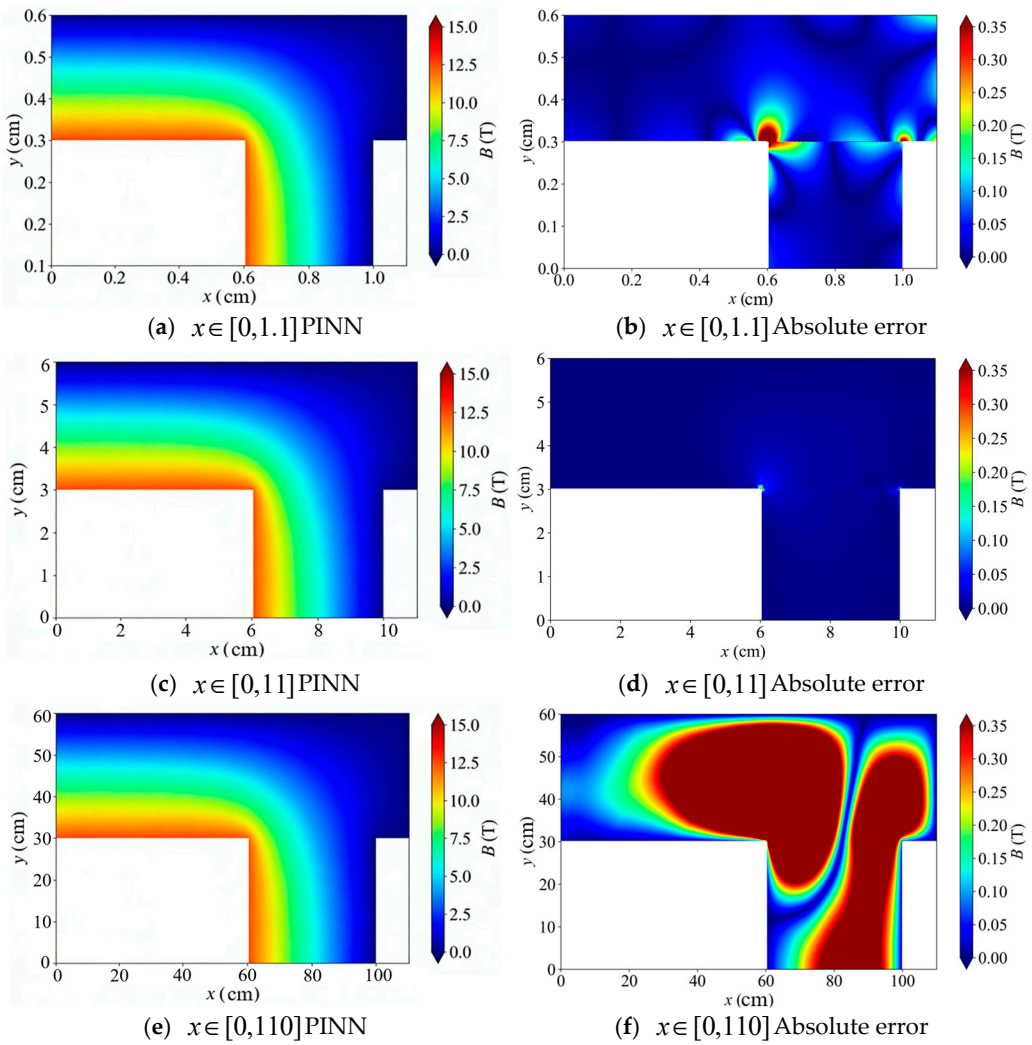


Figure 7. The simulations and analyses through PINN at different scales.

With the rail defined as the moving domain and the armature held stationary, the magnetic field distributions at t = 5 ms for velocities of 5 m/s, 10 m/s, 20 m/s, and 40 m/s have been comparatively analyzed using both the PINN and the FEM. The comparisons are conducted at the specified evaluation time of 5 ms for each velocity condition. These results represent the magnetic field distributions at a particular time instant and are intended to

assess the prediction accuracy of the proposed method in capturing the electromagnetic field characteristics and velocity skin effect under different prescribed velocities.

To quantitatively evaluate the magnetic field prediction accuracy, the maximum pointwise relative error is adopted as the error metric. For each velocity condition, the error is calculated using 1000 independent evaluation points at t = 5 ms. The absolute difference between the PINN-predicted magnetic flux density and the corresponding FEM reference value is normalized by the absolute FEM reference value at each evaluation point. The maximum of these pointwise relative errors is then expressed as a percentage, as defined below:

$$E_{\max} = \max_{1 \le j \le 1000} \left(\frac{\left| \hat{B}_z\left(x_j, t_j\right) - B_j \right|}{\left| B_j \right|} \right) \times 100\% \tag{31}$$

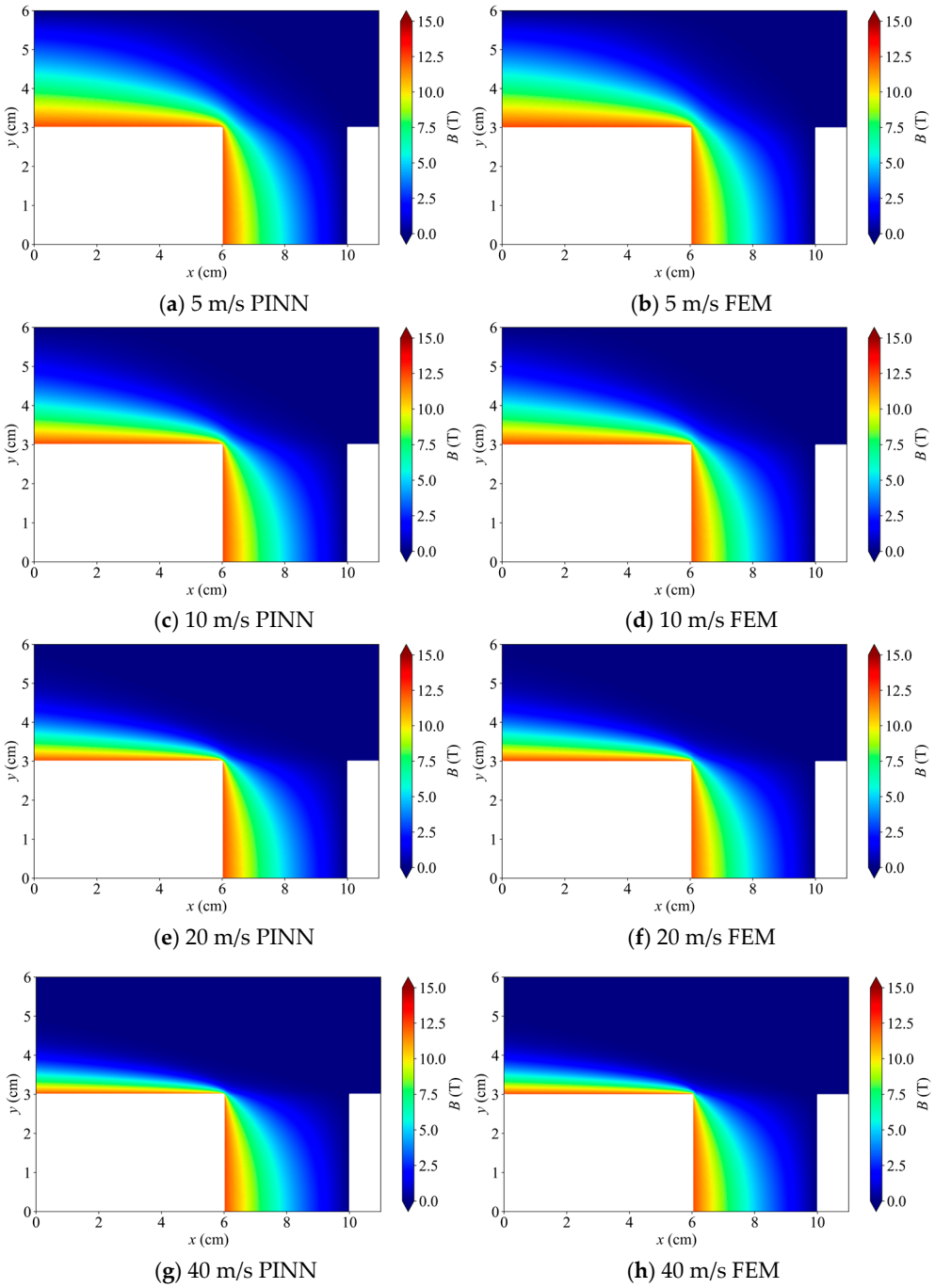
Here, $\hat{B}_z\left(x_j, t_j\right)$ and B_j denote the PINN-predicted and FEM reference magnetic flux densities at the j-th evaluation point, respectively. The normalization is performed using the corresponding FEM reference value at each evaluation point.

To ensure an independent assessment of prediction accuracy, 1000 evaluation points are selected separately from the 200 FEM reference points used for training under each velocity condition. The spatial coordinates of the two datasets are checked to ensure that no evaluation point coincides with a supervised training point. The FEM magnetic field values at these evaluation locations are used exclusively for comparison with the predictions of the trained network and are not included in the data-driven loss defined in Equation (29). Furthermore, the same independent evaluation point set is employed for different sampling strategies under each velocity condition, ensuring that the reported prediction errors are evaluated consistently.

As shown in Figure 8, the simulation results obtained from PINN and FEM demonstrate substantial agreement. In addition, it can be seen from the figure that the magnetic field intensity distribution shows obvious non-uniformity and concentrates at the edge of the conductor as the speed increases, which is consistent with the skin effect in electromagnetic theory. Specifically, under low-speed conditions (5 m/s, 10 m/s), the magnetic field still has a strong distribution inside the conductor, indicating that the current has not been completely transferred to the surface of the conductor, while under higher speed conditions (20 m/s, 40 m/s), the magnetic field is mainly concentrated on the surface of the conductor, and the current tends to flow on the surface. The higher the speed, the more the current distribution concentrates on the surface of the conductor, and concentrates on the edge of the conductor with the increase in the speed. The results conform to the prediction of the classical electromagnetic theory on the skin effect. Figure 9 shows the convergence results of the CVT-ND-PINN loss terms.

Figures 10 and 11, respectively, present the absolute error contour plots and the magnetic field distribution along the rail's bottom edge between FEM and PINN solutions at rail velocities of 5 m/s (a), 10 m/s (b), 20 m/s (c), and 40 m/s (d). The analysis reveals that the maximum error consistently concentrates at the armature's trailing edge. The largest absolute error consistently appears near the trailing edge of the armature, where the magnetic field gradient is strongest, and the local electromagnetic behavior is most difficult to approximate. In addition, the magnitude and concentration of this error increase systematically with velocity. This result indicates that the dominant source of prediction difficulty does not lie in the relatively smooth regions inside the computational domain, but rather in the highly localized electromagnetic structures generated by moving-conductor effects and the velocity skin effect. In these regions, the field redistributes rapidly over a narrow spatial range, creating a sharp convection–diffusion imbalance that is difficult for conventional PINN sampling strategies to capture. This observation provides a direct physical motivation for introducing adaptive collocation sampling. If collocation points are

distributed uniformly or purely randomly over the entire domain, the network inevitably allocates insufficient representational capacity to the most challenging local regions. Therefore, improving the spatial allocation of training points is essential for enhancing both local accuracy and global predictive performance.



(**a**) 5 m/s PINN (**b**) 5 m/s FEM

(**c**) 10 m/s PINN (**d**) 10 m/s FEM

(**e**) 20 m/s PINN (**f**) 20 m/s FEM

(**g**) 40 m/s PINN (**h**) 40 m/s FEM

Figure 8. Comparison of magnetic flux density distributions predicted by PINN and FEM at t = 5 ms under different velocities.

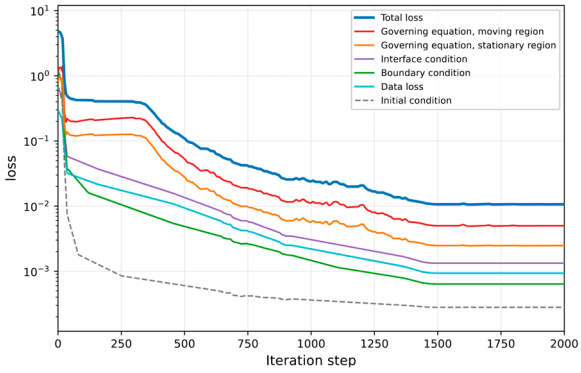
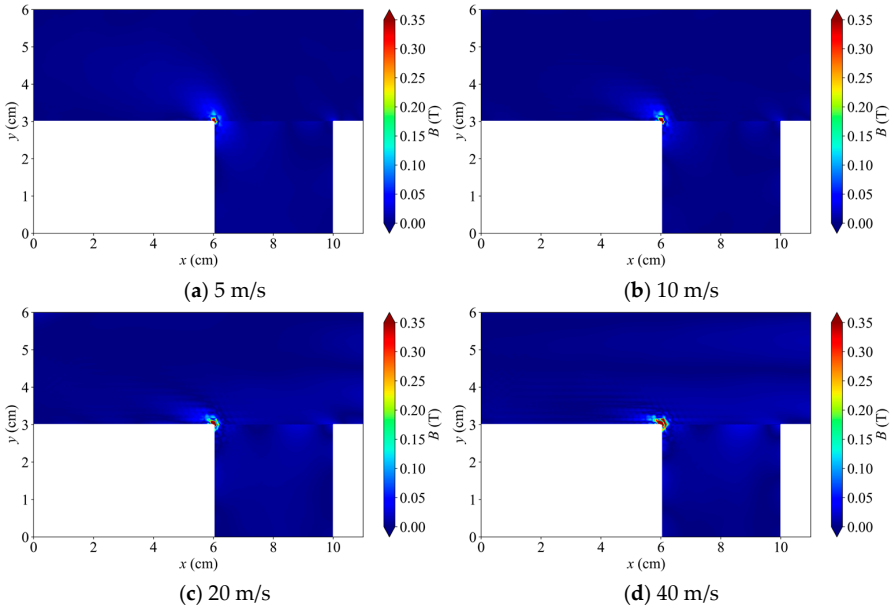


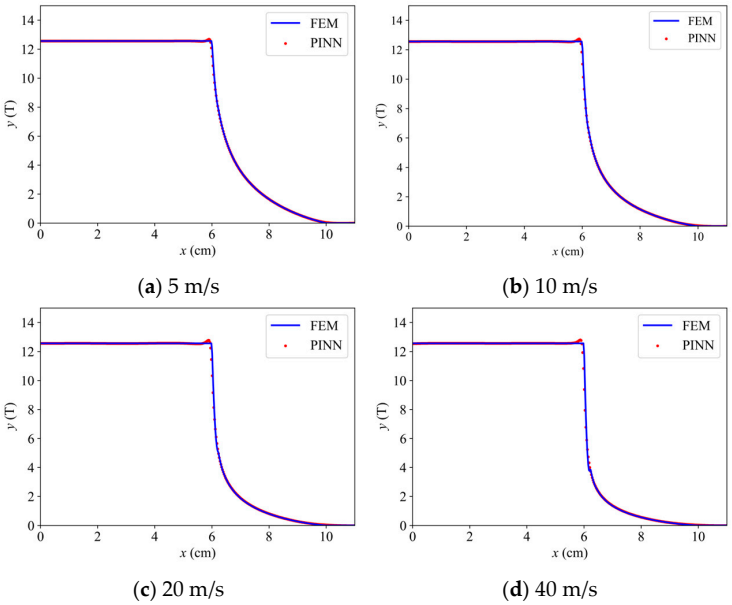
Figure 9. Convergence Results.



(**a**) 5 m/s (**b**) 10 m/s

(**c**) 20 m/s (**d**) 40 m/s

Figure 10. The distribution of absolute magnetic field errors at different speeds.



(**a**) 5 m/s (**b**) 10 m/s

(**c**) 20 m/s (**d**) 40 m/s

Figure 11. The magnetic field distribution at the bottom edge of the rail at different speeds.

To evaluate the computational efficiency, the computational times of FEM and CVT-ND-PINN (4000 collocation points) were compared at four velocities using an Intel Xeon Platinum 8369B CPU and an NVIDIA RTX 4060 Ti GPU. As shown in Table 5, GPU execution reduced the CVT-ND-PINN training time by approximately seven times compared with CPU execution, with GPU training times ranging from 1127 to 1193 s, comparable to the FEM computational times. Furthermore, the trained network required approximately 1.2 ms to predict the magnetic field at 1000 evaluation points, demonstrating its potential for rapid electromagnetic field prediction.

Table 5. Time results obtained by different methods.

Parameters	CPU Time	GPU Time
5 m/s (FEM)	1083 s	1041 s
10 m/s (FEM)	1126 s	1089 s
20 m/s (FEM)	1197 s	1152 s
40 m/s (FEM)	1296 s	1247 s
5 m/s (CVT-ND-PINN)	7926 s	1127 s
10 m/s (CVT-ND-PINN)	8015 s	1142 s
20 m/s (CVT-ND-PINN)	8183 s	1168 s
40 m/s (CVT-ND-PINN)	8342 s	1193 s

To evaluate the effectiveness of the proposed adaptive sampling mechanism, three collocation point generation strategies were compared: uniform sampling (US), random sampling (RS), and CVT adaptive sampling. The 3675 points in the localized region ($x \in [5.5,6.5]$, $y \in [2.5,3.5]$) are shown in Figures 12 and 13. In Figure 13, the red dots represent the collocation points generated by the respective sampling strategies, while the blue lines in the CVT panel indicate the boundaries of the Voronoi cells. While uniform sampling offers structural regularity, it fails to capture local singularities in regions with steep electromagnetic gradients due to insufficient point density. Although random sampling provides certain flexibility, its stochastic distribution often leads to a coexistence of under-sampling in critical regions and redundant sampling elsewhere, thereby exacerbating training instability and generalization errors. In contrast, the CVT strategy dynamically optimizes the sample distribution by automatically concentrating high-density collocation points in areas characterized by rapid field variations or geometric/physical singularities, particularly near the armature-rail interface and within the skin depth. Consequently, this approach significantly improves model convergence accuracy for a fixed total number of nodes.

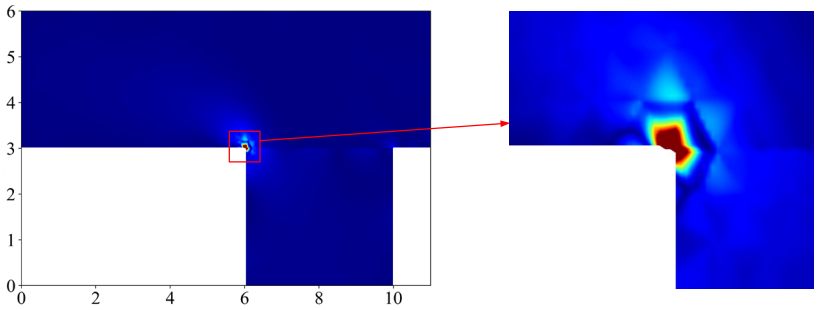
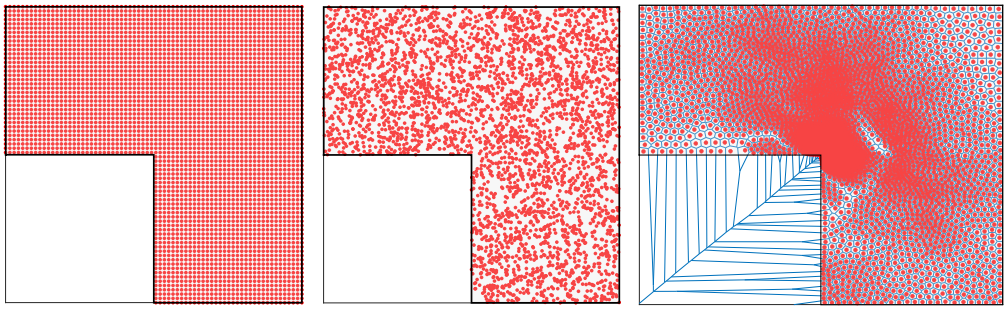


Figure 12. The localized error amplification.



(**a**) Uniform Sampling (**b**) Random Sampling (**c**) CVT

Figure 13. Comparison of Three Sampling Methods.

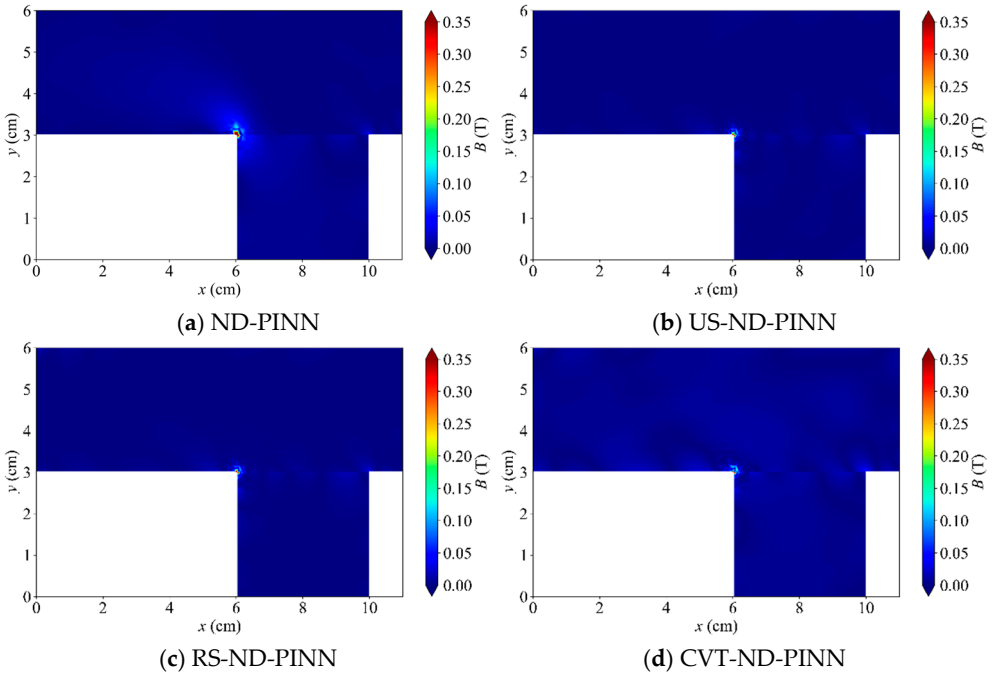
The proposed CVT-ND-PINN framework integrates spatiotemporal coordinate scaling, CVT adaptive sampling, and a supplemental local data-driven mechanism to address complementary challenges in electromagnetic field prediction. Coordinate scaling is employed to alleviate numerical optimization difficulties associated with different input coordinate scales, while CVT adaptive sampling redistributes collocation points toward high-gradient regions near the armature–rail interface and the trailing edge of the armature. In addition, the data-driven loss introduces supplementary reference magnetic field information to assist the approximation of complex local field distributions. These components are incorporated into a unified physics-informed learning framework, addressing the numerical representation of input variables, the spatial distribution of collocation points, and the incorporation of supplementary field constraints, respectively.

Figure 14 compares the magnetic field prediction error distributions obtained using different PINN configurations, illustrating the prediction performance associated with the investigated sampling strategies. This indicates that discrepancies between the predicted fields and the FEM reference solution are effectively suppressed, particularly in numerically unstable zones such as the armature-rail contact interface at the trailing edge. These observations are robustly corroborated by the quantitative data in Table 6; the CVT-ND-PINN framework consistently maintains the lowest maximum relative error across all tested velocities. Notably, at 40 m/s, the CVT-ND-PINN achieves a maximum relative error of 3.42%, corresponding to error reductions of approximately 62.7% and 61.3% compared with uniform and random sampling strategies, respectively, and approximately 80.1% compared with the baseline ND-PINN method. These results demonstrate that the synergistic interplay between CVT adaptive sampling and the local data-driven mechanism substantially enhances the model's spatial resolution accuracy for high-gradient fields and singularities, thereby enabling more stable and reliable magnetic field predictions under dynamic operating conditions.

It should be noted that Table 6 presents a comparison of different collocation sampling strategies, whereas Table 7 investigates the sensitivity of the CVT-ND-PINN method to the number of collocation points. Specifically, the relative error of 3.42% at 40 m/s in Table 6 is obtained from the sampling-strategy comparison, while the corresponding value of 3.51% in Table 7 is associated with the experiment using 2500 CVT collocation points. Therefore, these values represent results from different experimental comparisons and should not be directly interpreted as repeated measurements under identical training configurations.

Figure 15 shows the distribution of load points in the computational space based on the Centroidal Voronoi Tessellation (CVT) strategy, with point densities of 2500, 1500, 500, and 100 points in panels (a), (b), (c), and (d), respectively. In these plots, red dots represent the CVT-generated collocation points, while blue lines indicate the boundaries of the corresponding Voronoi cells. As the number of points decreases from 2500 to 100, the distribution becomes sparser, but the CVT method continues to ensure an efficient and

adaptive allocation. For 2500 points (a), the points are tightly clustered in high-gradient regions, such as the armature-rail interface, where the electromagnetic field varies sharply. Reducing the number of points in CVT1500 (b) and CVT500 (c) still provides a balanced distribution, capturing critical regions with fewer redundancies in smoother areas. Even with only 100 points (d), the CVT method adapts by placing more points in regions of higher error, ensuring the simulation focuses on areas with steep field gradients. This demonstrates that CVT adaptive sampling can maintain accuracy with fewer points, optimizing the point distribution while managing computational cost. These results highlight the flexibility of the CVT strategy in effectively adapting the point distribution for accurate solution capture and efficient error minimization.



(**a**) ND-PINN (**b**) US-ND-PINN

(**c**) RS-ND-PINN (**d**) CVT-ND-PINN

Figure 14. The distribution of magnetic field prediction errors under different sampling strategies.

Table 6. Comparison of maximum relative errors among various sampling strategies at different speeds.

Method	Maximum Relative Error			
	5 m/s	**10 m/s**	**20 m/s**	**40 m/s**
ND-PINN	5.47%	7.96%	11.70%	17.19%
Uniform Sampling-ND-PINN	2.47%	3.66%	5.57%	9.16%
Random Sampling-ND-PINN	2.31%	3.42%	5.25%	8.84%
CVT-ND-PINN	1.11%	1.51%	1.99%	3.42%

Table 7. Maximum relative errors of the CVT strategy across varying node counts and speeds.

Velocity	Maximum Relative Error			
	2500	**1500**	**500**	**100**
5 m/s	1.11%	1.19%	1.51%	2.07%
10 m/s	1.51%	1.67%	2.07%	2.95%
20 m/s	2.15%	2.39%	2.95%	4.38%
40 m/s	3.51%	3.58%	3.82%	6.61%

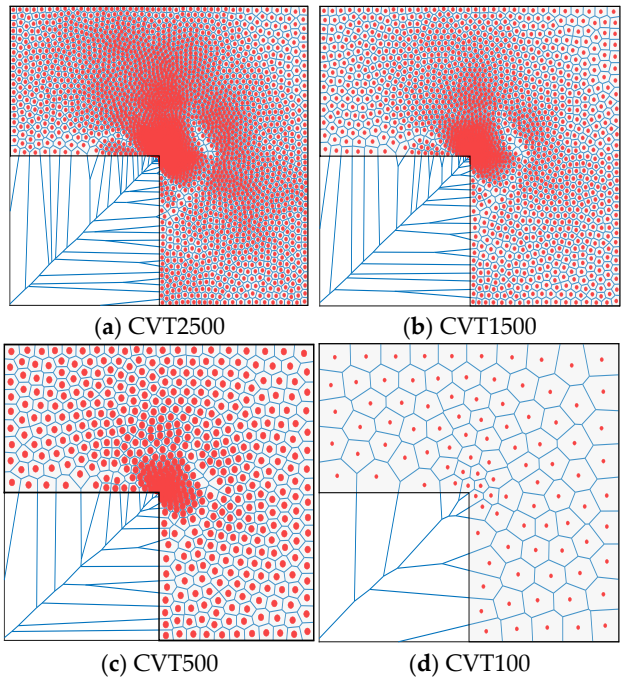


Figure 15. Distribution of load point space based on CVT strategy.

Figure 16 and Table 7 present the magnetic field error distributions and the relative errors for varying node counts and speeds using the CVT strategy. As the number of nodes decreases from 2500 to 100, the error distribution becomes more concentrated in regions with higher gradients, particularly near the armature-rail interface. In Figure 16a, the error is minimal, and the distribution is well resolved. However, as the number of nodes decreases in Figure 16b,c, the error slightly increases, though the method still effectively captures the main features of the magnetic field. In Figure 16d, with only 100 points, the error becomes more noticeable, especially in regions with sharp field gradients. The relative errors in Table 7 reveal that as the number of points decreases, the error increases, particularly at higher speeds. For 5 m/s, the error increases from 1.11% at 2500 points to 2.07% at 100 points. At 40 m/s, the error climbs significantly from 3.51% at 2500 points to 6.61% at 100 points. These results demonstrate the influence of the number of CVT collocation points on prediction accuracy and highlight the ability of the adaptive sampling strategy to capture localized high-gradient electromagnetic field characteristics using different sampling densities. Although the accuracy slightly decreases as the number of points is reduced, particularly at higher speeds, the CVT strategy still ensures that points are distributed where the field gradients are the steepest, optimizing the sampling for error minimization. This demonstrates that the CVT method remains highly effective in capturing key features of the solution, even with fewer points, ensuring accuracy.

To quantitatively evaluate the individual contributions of coordinate scaling, CVT adaptive sampling, and FEM-based supervision, a controlled ablation study was conducted using the complete CVT-ND-PINN framework as the reference. Three additional configurations were constructed by removing one component at a time while retaining the other two. Specifically, coordinate scaling was disabled by using the original dimensional spatiotemporal coordinates and the corresponding dimensional governing equations. When CVT adaptive sampling was removed, random sampling was employed while maintaining the same total number of collocation points. When FEM-based supervision was removed, the data-driven loss term in Equation (30) was excluded from network training. All configurations employed the same neural network architecture, learning-rate schedule, 2000 training iterations, and experimental conditions. The comparison was performed at 40 m/s and

t = 5 ms using the same collocation-point budget as the sampling-strategy comparison and the same 1000 independent evaluation points. The maximum pointwise relative error was adopted as the evaluation metric. The corresponding ablation results are summarized in Table 8.

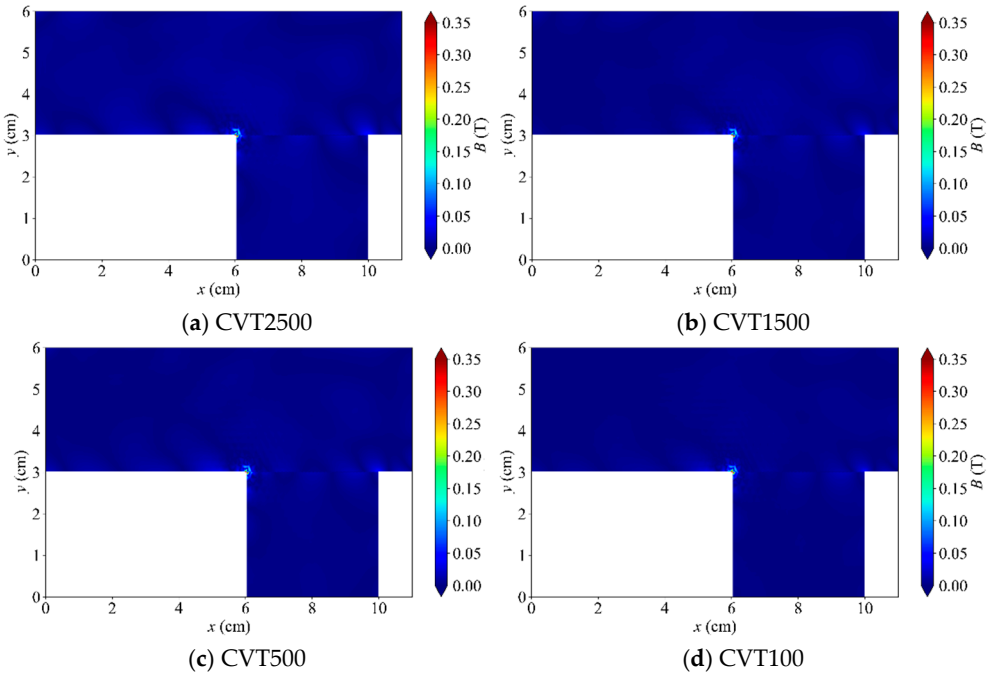


Figure 16. Comparison of absolute magnetic field prediction error distributions obtained using different CVT collocation-point budgets.

Table 8. The ablation experiment results of the CVT-ND-PINN framework at 40 m/s.

Configuration	Maximum Relative Error
Without coordinate scaling	7.26%
Without CVT sampling (random sampling)	8.84%
Without FEM-based supervision	5.93%
Complete CVT-ND-PINN	3.42%

As shown in Table 8, the complete CVT-ND-PINN framework achieves a maximum pointwise relative error of 3.42%. When coordinate scaling is removed, the error increases to 7.26%, corresponding to an increase of 3.84 percentage points, indicating that appropriate coordinate scaling contributes to reducing numerical scale disparities and improving prediction accuracy. Replacing CVT adaptive sampling with random sampling increases the error to 8.84%, an increase of 5.42 percentage points, demonstrating the effectiveness of adaptive collocation-point redistribution in resolving localized high-gradient electromagnetic fields. Furthermore, excluding FEM-based supervision increases the error to 5.93%, corresponding to an increase of 2.51 percentage points, indicating that supplementary FEM reference data improve the reconstruction of complex magnetic field distributions near the armature–rail interface. Among the three component-removal configurations, replacing CVT adaptive sampling produces the largest increase in prediction error. These results quantitatively demonstrate the contributions of the individual components within the integrated framework and support the effectiveness of combining coordinate scaling, CVT adaptive sampling, and FEM-based supervision.

To evaluate the statistical reliability of the proposed CVT-ND-PINN framework, five independent training runs were performed for each velocity condition of 5, 10, 20, and

40 m/s. Different random seeds were used while maintaining the same neural network architecture, learning-rate schedule, 2000 training iterations, CVT collocation-point budget, and FEM supervision data. All trained models were evaluated at t = 5 ms using the same set of 1000 independent evaluation points, and the maximum pointwise relative error was adopted as the evaluation metric. The statistical results show that the mean errors over the five independent runs at 5, 10, 20, and 40 m/s were 1.13%, 1.54%, 2.07%, and 3.48%, respectively, with corresponding standard deviations of 0.04, 0.06, 0.06, and 0.10 percentage points. The mean prediction error increases with velocity, which is consistent with the trend observed in the preceding single-run results. Meanwhile, the relatively small standard deviations across all investigated velocity conditions indicate that the proposed method exhibits good prediction repeatability under different random initializations.

5. Conclusions

This study proposed a Centroidal Voronoi Tessellation-based nondimensional physics-informed neural network for solving the electromagnetic field of the electromagnetic rail launch model under moving-conductor conditions. The proposed method was designed to address two major challenges in the electromagnetic rail launch model electromagnetic simulation: the severe optimization difficulty caused by strong multiscale spatiotemporal coupling, and the insufficient local resolution of conventional PINNs in regions dominated by the velocity skin effect. To overcome these issues, a nondimensionalization strategy was introduced, thereby improving training stability and numerical robustness. On this basis, a CVT adaptive collocation sampling strategy was further employed to redistribute collocation points toward regions with stronger field gradients and local singularity characteristics. By integrating these components within a physics-informed neural network framework, the proposed method provides an approximation of the electromagnetic field that incorporates the governing physical constraints and achieves good agreement with the FEM reference results under the investigated conditions. Comparative analysis with the finite element method (FEM) shows that the proposed framework significantly reduces prediction errors, particularly under 40 m/s, achieving a maximum relative error of only 3.42%. These results emphasize the effectiveness of the CVT strategy in ensuring high accuracy with fewer points and its ability to optimize point distribution in regions with steep electromagnetic gradients. Although the prediction error increases as the number of collocation points decreases, the CVT-ND-PINN framework maintains the ability to reproduce the main electromagnetic field characteristics with fewer sampling points, demonstrating the effectiveness of the CVT adaptive sampling strategy in resolving localized high-gradient regions. Looking ahead, future work will focus on extending the applicability of the PINN-based approach to more complex geometries, multi-physics coupling scenarios, and in-depth study of local data sampling area and quantity—thereby broadening its impact in the domain of engineering electromagnetics.

Author Contributions: Conceptualization, Y.S. and X.H.; methodology, Y.S. and H.X.; software, Y.S. and H.X.; validation, Y.S., J.F. and H.W.; formal analysis, Y.S. and J.F.; investigation, Y.S., H.X. and H.W.; resources, S.H. and X.H.; data curation, Y.S. and J.F.; writing—original draft preparation, Y.S.; writing—review and editing, H.X., S.H., X.H. and F.W.; visualization, Y.S. and J.F.; supervision, X.H. and F.W.; project administration, X.H.; funding acquisition, X.H. and F.W. All authors have read and agreed to the published version of the manuscript.

Funding: This research was funded by the Innovation Ability Cultivation Support Project for Graduate Students in Hebei Province (CXZZBS2025066), the National Natural Science Foundation of China (grant number 92266203), and the Science & Technology Program of Hebei (SJMYF202507).

Data Availability Statement: The raw data supporting the conclusions of this article will be made available by the authors on request.

Conflicts of Interest: The authors declare that they have no known competing financial interests or personal relationships that could have appeared to influence the work reported in this paper.

References

1. Lou, Y.; Li, H.; Li, B. Research on proximity effect of electromagnetic railgun. *Def. Technol.* **2016**, *12*, 223–226. [CrossRef]
2. Li, B.; Lin, Q. Analysis and discussion on launching mechanism and tactical electromagnetic railgun technology. *Def. Technol.* **2018**, *14*, 484–495. [CrossRef]
3. Zhu, C.; Li, B. Analysis of sliding electric contact characteristics in augmented railgun based on the combination of contact resistance and sliding friction coefficient. *Def. Technol.* **2020**, *16*, 747–752. [CrossRef]
4. Wu, K.; Wu, W.; Pan, A.; Guo, C.; Cui, F.; Yang, X.; Yang, G. Investigation on the microstructure evolution and mechanical properties of electromagnetic rail material in a launch environment. *Mater. Charact.* **2024**, *208*, 113582. [CrossRef]
5. Pang, Z.; Wang, H.; Wang, H.; Zhang, L. Analysis of current and magnetic field distributions in rail launcher with Peaceman–Rachford finite-difference method. *IEEE Trans. Plasma Sci.* **2012**, *40*, 2717–2722. [CrossRef]
6. Zhou, P.; Li, B. Numerical calculation of magnetic–thermal coupling and optimization analysis for velocity skin effect. *IEEE Trans. Plasma Sci.* **2021**, *49*, 3994–4001. [CrossRef]
7. Ghassemi, M.; Barsi, Y.M. Effect of liquid film (indium) on thermal and electromagnetic distribution of an electromagnetic launcher with new armature. *IEEE Trans. Magn.* **2005**, *41*, 408–413. [CrossRef]
8. Yin, Q.; Zhang, H.; Li, H.; Yang, Y. Analysis of in-bore magnetic field in c-shaped armature railguns. *Def. Technol.* **2019**, *15*, 83–88. [CrossRef]
9. Karpagam, R.; Lydia, J.; Murugan, R.; Kumar, C.R. Understanding the behaviour of magnetic field distribution of railgun under transient conditions using finite element method. *Meas. Sens.* **2024**, *31*, 100971. [CrossRef]
10. Lei, J.; Liu, W.; Yu, Y.; Luo, Z. A numerical simulation method for solving electromagnetic-mechanical coupling field. *J. Eng. Res.* **2024**, *13*, 1127–1139. [CrossRef]
11. Gu, B.; Li, H.; Li, B. An internal ballistic model of electromagnetic railgun based on PFN coupled with multi-physical field and experimental validation. *Def. Technol.* **2024**, *32*, 254–261. [CrossRef]
12. Zhang, B.; Kou, Y.; Jin, K.; Zheng, X. A multi-field coupling model for the magnetic-thermal-structural analysis in the electromagnetic rail launch. *J. Magn. Magn. Mater.* **2021**, *519*, 167495. [CrossRef]
13. Zhang, B.; Kou, Y.; Jin, K.; Zheng, X. Dynamic response of electromagnetic railgun under time-dependent electromagnetic moving loads. *J. Sound Vib.* **2020**, *483*, 115451. [CrossRef]
14. Raissi, M.; Perdikaris, P.; Karniadakis, G.E. Physics-informed neural networks: A deep learning framework for solving forward and inverse problems involving nonlinear partial differential equations. *J. Comput. Phys.* **2019**, *378*, 686–707. [CrossRef]
15. Wang, S.; Sankaran, S.; Stinis, P.; Perdikaris, P. Simulating Three-dimensional Turbulence with Physics-informed Neural Networks. *arXiv* **2025**, arXiv:2507.08972. [CrossRef]
16. Kamil, H.; Soulaïmani, A.; Beljadid, A. A transfer learning physics-informed deep learning framework for modeling multiple solute dynamics in unsaturated soils. *Comput. Methods Appl. Mech. Eng.* **2024**, *431*, 117276. [CrossRef]
17. Pinto, G.; Messina, R.; Li, H.; Hong, T.; Piscitelli, M.S.; Capozzoli, A. Sharing is caring: An extensive analysis of parameter-based transfer learning for the prediction of building thermal dynamics. *Energy Build.* **2022**, *276*, 112530. [CrossRef]
18. Fang, Z.; Zhan, J. Deep physical informed neural networks for metamaterial design. *IEEE Access* **2020**, *8*, 24506–24513. [CrossRef]
19. Cai, S.; Wang, Z.; Wang, S.; Perdikaris, P.; Karniadakis, G.E. Physics-informed neural networks for heat transfer problems. *J. Heat Transf.* **2021**, *143*, 060801. [CrossRef]
20. Cai, S.; Mao, Z.; Wang, Z.; Yin, M.; Karniadakis, G.E. Physics-informed neural networks (PINNs) for fluid mechanics: A review. *Acta Mech. Sin.* **2021**, *37*, 1727–1738. [CrossRef]
21. Zhang, E.; Dao, M.; Karniadakis, G.E.; Suresh, S. Analyses of internal structures and defects in materials using physics-informed neural networks. *Sci. Adv.* **2022**, *8*, eabk0644. [CrossRef] [PubMed]
22. Chen, J.; Pierce, J.; Williams, G.; Simpson, T.W.; Meisel, N.; Narra, S.P.; McComb, C. Accelerating thermal simulations in additive manufacturing by training physics-informed neural networks with randomly synthesized data. *J. Comput. Inf. Sci. Eng.* **2024**, *24*, 1–14. [CrossRef]
23. Khan, A.; Lowther, D.A. Physics informed neural networks for electromagnetic analysis. *IEEE Trans. Magn.* **2022**, *58*, 7500404. [CrossRef]
24. Noakoasteen, O.; Wang, S.; Peng, Z.; Christodoulou, C. Physics-informed deep neural networks for transient electromagnetic analysis. *IEEE Open J. Antennas Propag.* **2020**, *1*, 404–412. [CrossRef]

25. Beltran-Pulido, A.; Bilionis, I.; Aliprantis, D. Physics-informed neural networks for solving parametric magnetostatic problems. *IEEE Trans. Energy Convers.* **2022**, *37*, 2678–2689. [CrossRef]
26. Gong, R.; Tang, Z. Hot Spot Driven Physics-informed Neural Network via Special Designed Quantity of Interest applied to Magneto-thermal Analysis. In Proceedings of the 2022 IEEE 20th Biennial Conference on Electromagnetic Field Computation (CEFC), Denver, CO, USA, 24–26 October 2022; pp. 1–2.
27. Qi, S.; Sarris, C.D. Electromagnetic-thermal analysis with FDTD and physics-informed neural networks. *IEEE J. Multiscale Multiphysics Comput. Tech.* **2023**, *8*, 49–59. [CrossRef]
28. Jeong, Y.; Jo, J.; Lee, T.; Yoo, J. Combined analysis of thermofluids and electromagnetism using physics-informed neural networks. *Eng. Appl. Artif. Intell.* **2024**, *133*, 108216. [CrossRef]
29. Pu, H.; Tan, B.; Yi, J.; Yuan, S.; Zhao, J.; Bai, R.; Luo, J. A novel key performance analysis method for permanent magnet coupler using physics-informed neural networks. *Eng. Comput.* **2024**, *40*, 2259–2277. [CrossRef]
30. Hou, S.; Hao, X.; Pan, D.; Wu, W. Physics-informed neural network for simulating magnetic field of coaxial magnetic gear. *Eng. Appl. Artif. Intell.* **2024**, *133*, 108302. [CrossRef]

Disclaimer/Publisher's Note: The statements, opinions and data contained in all publications are solely those of the individual author(s) and contributor(s) and not of MDPI and/or the editor(s). MDPI and/or the editor(s) disclaim responsibility for any injury to people or property resulting from any ideas, methods, instructions or products referred to in the content.